 doi:10.20944/preprints202210.0176.v1

Article

Aerosol Mineral Dust Pollution over Nicosia, Cyprus, April 2019

Yuliia Yukhymchuk [1,2], Gennadi Milinevsky [1,3,4,*], Ivan Syniavskyi [1], Ioana Popovici [2,5], Florin Unga [6,7], Jean Sciare [6], Franco Marenco [6], Michael Pikridas [6], and Philippe Goloub [2]

1 Department for Atmospheric Optics and Instrumentation, Main Astronomical Observatory, 03143 Kyiv, Ukraine; yuliia.yukhymchuk@mao.kiev.ua (Y.Y.); syn@mao.kiev.ua (I.S.)
2 Laboratoire d'Optique Atmosphérique, Centre National de la Recherche Scientifique (CNRS), University of Lille, 59000 Lille, France; philippe.goloub@univ-lille.fr (P.G.)
3 International Center of Future Science, College of Physics, Jilin University, 130012 Changchun, China
4 Physics Faculty, Taras Shevchenko National University of Kyiv, 01601 Kyiv, Ukraine; gennadi.milinevsky@knu.ua (G.M.)
5 Research &Development Department, Cimel Electronique, 75011 Paris, France; i-popovici@cimel.fr (I.P.)
6 Climate and Atmosphere Research Centre (CARE-C), The Cyprus Institute, 2121 Nicosia, Cyprus; j.sciare@cyi.ac.cy (J.S.); m.pikridas@cyi.ac.cy (M.P.); f.marenco@cyi.ac.cy (F.M.)
7 National Research Council of Italy, Institute of Atmospheric Sciences and Climate (CNR-ISAC), 73100 Lecce, Italy; f.unga@isac.cnr.it (F.U.)
* Correspondence: gennadi.milinevsky@knu.ua, genmilinevsky@gmail.com; Tel.: +380-67-209-6256

Abstract: The climate change impacts on some regions of the planet faster and stronger. These areas are known as the hot spots for climate change and Cyprus (Nicosia) in the Mediterranean is one of these spots. This paper aims to analyze the significant changes of atmospheric aerosol characteristics in 2019 and during the extreme event of 25 April 2019. We study the aerosol optical thickness (AOT), Ångström exponent, single scattering albedo, refractive index (imaginary and real parts), size, and vertical distribution of aerosol particles during the event of a high atmospheric aerosol contamination over Nicosia in details. For this purpose, we used the ground-based lidar, observations of the sun-photometer AERONET Nicosia station, satellite products from the Moderate Resolution Imaging Spectroradiometer (MODIS), and back trajectories of air movements calculated using the Hybrid Single Particle Lagrangian Integrated Trajectory Model (HYSPLIT). On 23–25 April, according to lidar and sun-photometer observations, strong aerosol pollution over Nicosia was detected. On April 25, 2019, the AOT value exceeds 1.0 at λ = 440 nm. Analysis of the optical and microphysical characteristics supported that the pollution consists of mainly Saharan dust and partly urban aerosols. This assumption was confirmed by HYSPLIT backward trajectories and MODIS images where air masses containing dust particles came from North Africa and from the Eastern part of Europe.

Keywords: aerosol; AERONET; lidar; air pollution; sun-photometer

1. Introduction

Aerosol particles in the atmosphere are one of the less known components of the atmosphere, that impact on human health and the global climate. According to the Fifth Assessment Report of the Intergovernmental Panel on Climate Change [1], aerosol-cloud interactions show the largest uncertainties reached, of 0.5 Wm^{-2}, in the estimating changes of the Earth energy budget. Direct aerosol impact on the energy budget in the Earth's atmosphere occurs due to scattering and absorbing solar radiation [2]. The indirect effect consists of the interaction between aerosols and clouds: aerosol particles act as cloud condensation nuclei and ice nuclei [3]. Aerosols can change droplet size, droplet concentration in the cloud, alter the cloud radiative properties.

There are some regions on the planet that are especially responsive to global warming and are exposed to greater risk than other regions. They are known as climate change

Preprints (www.preprints.org) | NOT PEER-REVIEWED | Posted: 12 October 2022 doi:10.20944/preprints202210.0176.v1

hotspots [4]. Cyprus Island located in the Eastern Mediterranean is one of these hotspots [5]. The Middle East type of a climate of this area is mostly dry and with prevailing hot weather [6]. Nicosia, the capital of Cyprus is located 149 m above sea level, is influenced by the local steppe climate. This climate is hot semi-arid with the average annual temperature ~20.0°C and precipitation amount ~360 mmv [7]. Providing research at the climate hotspots is significant for understanding the climate change impact on the regions where the global temperatures increase faster than in some others [1]. This data can be used for predicting and modeling climate changes.

Cyprus is affected by a mixture of various aerosol types such as dust particles from deserts, biomass burning aerosol from the North, and anthropogenic pollution from urban southeastern Europe and certainly, marine aerosols could be observed over the island [6]. The Cyprus Island also is under high risk of forest fires. High temperatures with the drought periods lead to the ignition and spreading of forest fires, particularly in summer. The highest risk is in June and July [6]. Besides smoke particles, mineral dust from the Saharan desert and deserts in the Middle East could be transported to Cyprus. It is known that the Saharan desert is one of the largest sources of mineral dust. The particles from this area could be transported for thousands of kilometers [8]. The mineral dust pollution from the Saharan desert was detected in different parts of the world and studied in many papers. For example, Saharan desert dust was detected over the southeastern United States [8]. The results of the detection of mineral dust in Northern, Southern and Eastern Europe can be found in [9–12]. The contamination of the Cyprus atmosphere by Saharan dust outbreaks over Nicosia was studied by Amiridis et al. [13], and Papayannis et al. [14]. The lidar aerosol studies for the eastern Mediterranean were presented by Nisantzi et al. [15] and Mamali et al. [16].

In this paper, we study the event of high aerosol contamination over Cyprus area, which took place in April 2019. The pollution event on date of 25 April 2019 is discussed in detail. Our analysis is based on the sun-photometer and lidar observations accompanied by MODIS satellite data and the HYSPLIT backward trajectories calculations. Section 2 describes the instruments and methods used in the work. Section 3 contains the observation results, backward trajectories calculations and discussion, followed by conclusions in Section 4.

2. Data and Methods

2.1. AERONET Sun-Photometer Station

The international network of automatic AERONET (AErosol RObotic NETwork) CIMEL CE318 sun-photometers [17] is one of the most advanced remote sensing aerosol monitoring systems [18, 19, 20]. The AERONET network is operated by NASA (USA) and the French and Spanish ACTRIS (Aerosols Clouds and TRace gas InfraStructure) components in Europe, and includes several hundred stations (about ~600) around the world. The tools of this network allow obtaining long-term series for the accurate aerosol parameters, that can be used for the analysis of the aerosol particle variations [21, 22, 23], studying the seasonal dynamics and the local aerosol behavior.

Accuracy of aerosol retrievals about ~0.01 Aerosol Optical Depth (AOD) provided by the AERONET network depends on sun-photometer calibration. The calibration consists of two parts: AOD and sky radiance measurements [24, 25]. Direct Sun Calibration includes the determination of the calibration coefficients. These coefficients are needed to convert the instrument digital output to the desired scientific output. Instruments are returned to the laboratory for intercomparison with reference instruments approximately every 12 months. For aerosol parameters analysis in this paper, we use the aerosol Version 2 direct sun algorithm [24] level 1.5 and level 2.0 parameters from the AERONET database: daily data, daily averages of AOD at 440 and 870 nm, and the Ångström exponent (AE) values computed using the 440 and 870 nm spectral channels, refractive index (RI), single scattering albedo (SSA).

Preprints (www.preprints.org) | NOT PEER-REVIEWED | Posted: 12 October 2022 doi:10.20944/preprints202210.0176.v1

Figure 1. Location of the AERONET station Nicosia at the Cyprus Atmospheric Observatory (CAO) station in Nicosia, Cyprus. Latitude: 35.14063°N, longitude: 33.38135°E, elevation: 181 m a.s.l. [25].

The sun-photometer of the Nicosia station is located at the Cyprus Atmospheric Observatory (CAO) in Nicosia (Figure 1.) in the Cyprus Institute at the Athalassa campus, in Aglantzia [26]. The station is equipped with the CE318NE sun-photometer from Cimel Electronique [17]. The sun-photometer is located on the roof of the building of the Cyprus Institute, which is located in the industrial area, about 5 km south of the Nicosia city center.

2.2. Lidar Measurements

The Lidar (Light Detection and Ranging) is a remote sensing instrument that uses a pulsed laser light for range and distance measuring in direction from satellite to the Earth surface [27] or from the Earth to some obstacles. Lidar instruments are the most powerful tools for observing the vertical properties of atmospheric aerosol. The principle of operation of the lidar does not differ much from radar: the directed light from the radiation source is reflected, and captured by a lidar sensor. Response time is directly proportional to the distance to the obstacle. In addition to the pulsed method of measuring the distance, the phase method is using. That method is based on determining the phase difference of the submitted and received signals. Light waves scatter in any medium, including air. Therefore, it is possible to detect the light scattering intensity in a transparent medium.

The CAO (location is shown in Figure 1) had also installed a CE370 micropulse lidar [28] from Cimel Electronique in the period 2018-2020. The CE370 lidar is a mono-wavelength elastic lidar operating at 532 nm, with no polarization channel.

2.3. MODIS/Terra/Aqua Spectroradiometer

The Moderate Resolution Imaging Spectroradiometer (MODIS) is a space instrument aboard the Terra (known as EOS AM-1) and Aqua (known as EOS PM-1) satellites [29]. The observations are available in near real-time and for almost global coverage because MODIS/Terra and MODIS/Aqua are observing the entire Earth's atmosphere/surface every 1 to 2 days. Instrument provides data in 36 spectral bands, or groups of wavelengths [30]. MODIS and other instruments onboard the Terra and Aqua satellite platforms data are transferred to ground stations in White Sands, New Mexico. After that, data are sent to the Goddard Space Flight Center for the EOS Data and Operations System (EDOS) for Level-0 processing. The next step is producing Level 1A, Level 1B, geolocation, and cloud mask products by the Goddard Earth Sciences Data and Information Services Center (GES DISC). In our work, we use the ability of MODIS to detect forest fire, volcanic eruptions and transboundary dust air pollution (e.g., [31]).

Preprints (www.preprints.org) | NOT PEER-REVIEWED | Posted: 12 October 2022 doi:10.20944/preprints202210.0176.v1

2.4. HYSPLIT Model

The Hybrid Single-Particle Lagrangian Integrated Trajectory model (HYSPLIT, [32]) is one of the most widely used models for calculations of atmospheric air masses backward trajectories. The model calculation method is a hybrid between the Lagrangian approach (calculations of the trajectories or air move) and the Eulerian methodology (connected with computing air pollutants) [33]. HYSPLIT can use a large variety of meteorological model data in its calculations, ranging from mesoscale to global scales. The calculation of forward and backward trajectories allows studying the transport of pollutants over different spatial and temporal ranges [33].

In our research, for backward trajectories building, we use the HYSPLIT model with the meteorological data files from The National Oceanic and Atmospheric Administration (NOAA) Global Data Assimilation System (GDAS). GDAS contains different meteorological data such as surface observations, satellite observations, wind profiler data, balloon data, radar observations, aircraft reports. The NOAA Global Forecast System (GFS) model used GDAS to place observations into a gridded model space for starting or initializing weather forecasts with observed data [34].

3. Results and discussion

This section contains the observation results and analyses of the optical and micro-physical properties of aerosols particles by sun-photometer measurements of the AERONET network (Subsection 3.1), spatial distribution of aerosols particles in the atmosphere over Nicosia (Cyprus) by the lidar sensing (Subsection 3.2), satellite images from MODIS and backward air mass transport trajectories made using HYSPLIT model (Subsection 3.3).

3.1. AERONET sun-photometer observations

3.1.1. Optical characteristics of aerosol particles

The optical aerosol characteristics such as aerosol optical depth (AOD), Ångström exponent (AE), and single scattering albedo (SSA) provide information about the type of aerosol particles. The first sun-photometer observation at the Nicosia station dates from 2015 according to the AERONET website. We considered the limited data for the specific periods in 2015 and 2016, and annual observations for 2019–2021 (Figure 2). The annual variation of AOD in the atmosphere over Nicosia shows the lowest concentration of aerosol particles during the winter season. From the beginning of spring, AOD values start to increase and vary until the end of autumn.

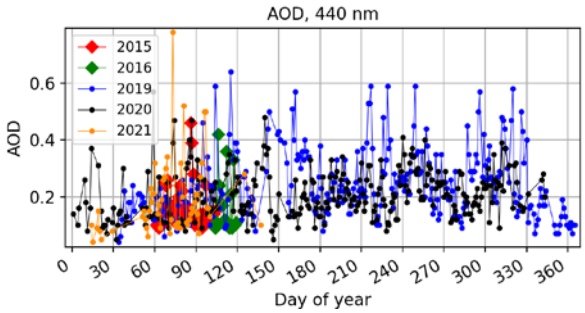

Figure 2. Changes aerosol optical depth during 2015–2021 years, Nicosia, Cyprus. The AERONET sun-photometer observations. Data level 2.0.

Furthermore, in 2015 and 2016, the AOD values are smaller than in the same period of 2019–2021. The data for 2021 at level 2.0 is available only for winter-spring period. The Ångström Exponent (AE) demonstrates the dominant size particles during observations. The computation of AE requires AOD at different wavelengths. This value shows the

Preprints (www.preprints.org) | NOT PEER-REVIEWED | Posted: 12 October 2022 doi:10.20944/preprints202210.0176.v1

connection between aerosol optical depths and their spectral dependence. AE depends on the size of particles, and it is one of the main characteristics of different aerosol types.

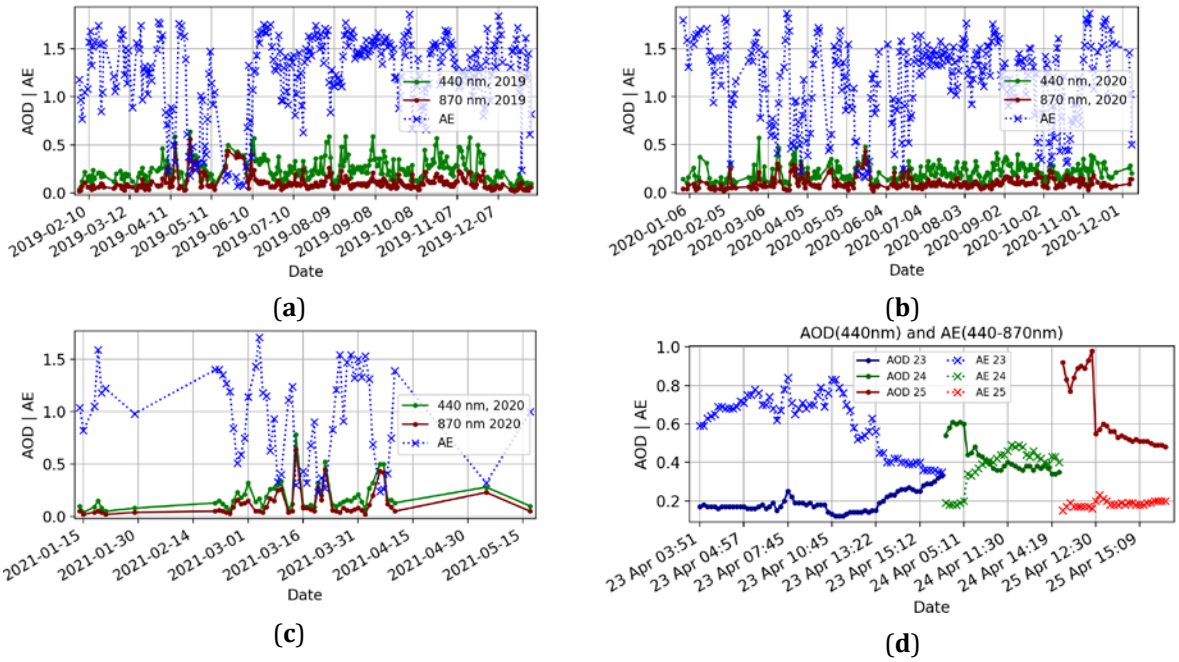

Figure 3. Changes in aerosol optical depth (AOD) and Ångström Exponent (AE) (470–870 nm) during (a) 2019, (b) 2020 and (c) 2021; (d) changes in AOD and AE (470–870 nm) during 23–25 April 2019, Nicosia, Cyprus. The AERONET sun-photometer observations. Data level 2.0.

The annual variations of the AOD and AE values are shown in Figure 3(a-c). During 2019–2021, the AOD and AE variations have a similar structure without strong season dependence. In the winter and early spring (approximately until April), AOD is lower than in the May–November period for 2019 and 2020 years. For 2021, few peaks with AOD around 0.5 were observes in March. However, others values were lower. In 2019, AOD peaks in summer and autumn were higher in comparison to 2020. In addition, annual AOD values in 2019 are larger than in the following year, especially in the spring season (Figures 2 and 3a-c). This effect could be connected to the COVID-19 pandemic and following a decrease in the industrial pollution. Furthermore, the AE data exhibit seasonal variations when the decrease was observed from the middle of spring to the beginning of summer. This period in Nicosia usually corresponds to the mineral dust transport from Sahara Desert areas.

Increased average daily AOD value at 440 nm ~0.64 was observed on 24 April 2019. However, separate measurements during the day show even higher AOD values up to ~0.8–1.0 (Figure 3d, red line). The daily averaged AOD maximum at 870 nm was of 0.56 (Figure 3a). During 23–25 April 2019 the AOD raised from 0.2 to ~0.8 (Figure 3d). The AOD increasing indicates the arrival of significant aerosol pollution in the atmosphere over Nicosia. This also was confirmed by the AE value changes, which decreased from 0.7 to less than 0.2 (Figure 3a, d). The AE variations anticorrelate with the AOD values (Figure 3a, d). The light blue line on 23 April shows that the AE from 0.6–0.8 diminished to 0.4–0.5 on 24 April (Figure 3d, light green line). On 25 April sun-photometer detected the lowest AE values of 0.1–0.2 (the pink curve in Figure 3d), which indicate the arrival of coarse mode particles in the atmosphere.

Preprints (www.preprints.org) | NOT PEER-REVIEWED | Posted: 12 October 2022 doi:10.20944/preprints202210.0176.v1

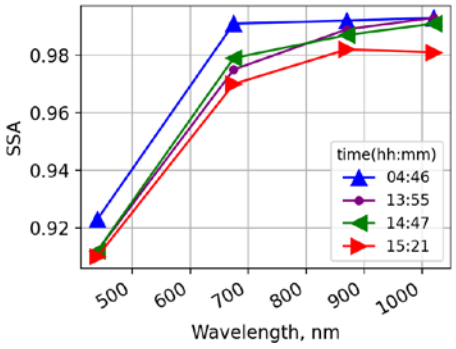

Figure 4. The single scattering albedo (SSA) on 25th April 2019, AERONET data from Nicosia, Cyprus. Data level 2.0.

SSA depends on absorbing and scattering characteristics of aerosol particles. According to data in Figure 4, the high SSA values were detected on 25 April 2019. In the morning at 4:46 UTC (Figure 4, blue line) SSA at 870 1020 nm wavelengths was close to 1. This means the domination of aerosols with mostly scattering properties. During the day, SSA values declined (green, yellow and red lines, Figure 4) which can be caused by dust mixed with other types of pollutants with absorbing properties. However, this impact is small and is probably connected with the daily pollution in that area, like traffic emissions in the evening time (corresponds to red line at 15:21 UTC in Figure 4).

3.1.2. Microphysical characteristics of aerosols particles

In this section, we consider microphysical aerosol characteristics: size distribution and refractive index. These properties can be obtained using a joint sun-photometer AOD and radiance inversion scheme [21] operationally applied in the AERONET network.

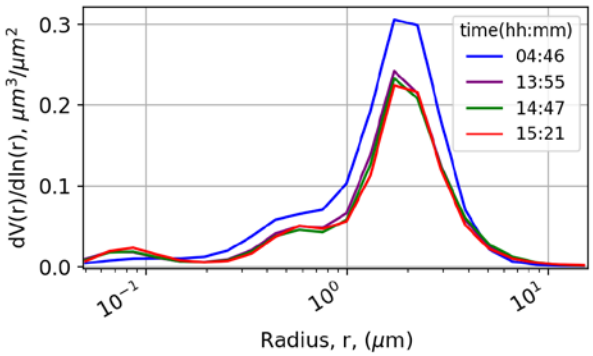

Figure 5. AERONET observations: aerosol size distribution on April 25, 2019, Nicosia, Cyprus. Data level 2.0.

Aerosols particles have a quite wide range of sizes: from the smallest with one-tenth of microns to the largest with a size of hundreds of micrometers. Conditionally whole aerosol fraction could be separated into coarse and fine modes. Each mode can correspond to a different aerosol type. According to size distribution, coarse mode was dominant on 25 April 2019 (Figure 5). In Figure 5, the large proportion of aerosols varies in size ranging from 1 to 10 micrometers with higher values in the morning at 4:46 and 5:37 UTC (red and blue lines, Figure 5) than in the afternoon. During the day the coarse mode concentration decreased, however the size distribution does not change. This type of distribution with the dominated coarse mode is typical for mineral dust pollution [35,36].

Preprints (www.preprints.org) | NOT PEER-REVIEWED | Posted: 12 October 2022 doi:10.20944/preprints202210.0176.v1

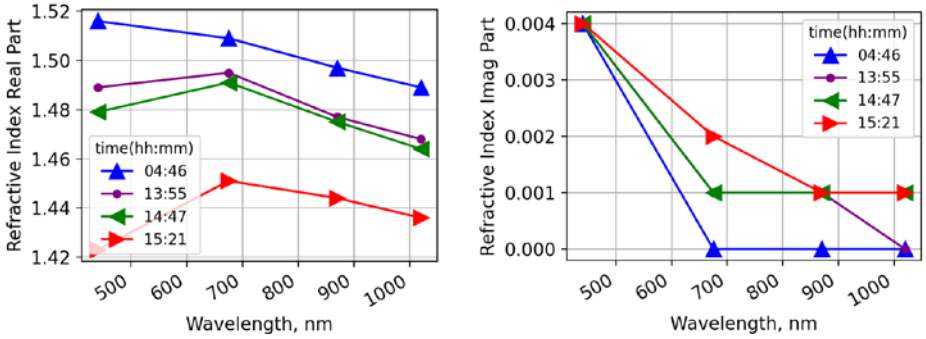

(**a**) (**b**)

Figure 6. Refractive index: (**a**) real part of the refractive index, (**b**) imaginary part of the refractive index on 25 April 2019, Nicosia, Cyprus. Data level 2.0.

The refractive index (RI) of aerosol particles, which is consisted of two parts, real and imaginary, is connected to the particles properties and types. The scattering aerosol property impacts on real part and the absorbing ability is responsible for imaginary part of refractive index values. The AERONET data of both parts of the refractive index for April 25, 2019 are presented in Figure 6. The RI real part values are in the range of 1.43–1.52 (Figure 6a), the values and variations with wavelengths are typical for mineral dust particles [36]. A similar result is obtained for the RI imaginary part. Firstly, the RI imaginary part is in a range less than 0.004, which means the low presence of absorbing particles (Figure 6b). Secondly, the shape of the variations of the RI imaginary part with wavelengths describes the changes matched with mineral dust [36].

3.1.3. Cluster analysis for aerosols particles type

The cluster analysis method allows to group data in datasets with similar characteristics. In the case of 23–25 April events, we have enough AOD and AE measurements to provide the cluster analysis of aerosol type particles [37, 38]. The changes in aerosol types are shown in the cluster diagram in Figure 7. The image shows the changes in dominant aerosol type in the atmosphere over Nicosia. For 2 days the anthropogenic pollution was switched to the aerosol with mineral dust features. The situation with pollution changed quickly but smoothly, therefore the contamination wasn`t spontaneous and could be moved to Nicosia with air mass transport from the distant sources.

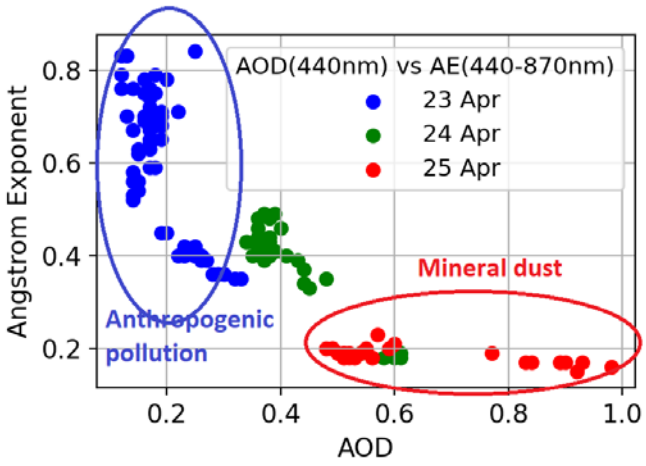

Figure 7. Cluster analysis for aerosol optical depth versus Ångström Exponent (470–870 nm) dependency during 23–25 April 2019, Nicosia, Cyprus. AERONET data. Data level 2.0.

Preprints (www.preprints.org) | NOT PEER-REVIEWED | Posted: 12 October 2022 doi:10.20944/preprints202210.0176.v1

3.2. Lidar observations

Lidar observations provide information on the altitude distribution of aerosols particles with high spatial resolution. In contrast to AERONET observations, which retrieve aerosol characteristics for a whole atmospheric column, lidar observations allow defining the altitudes of particles, spatial structure [14].

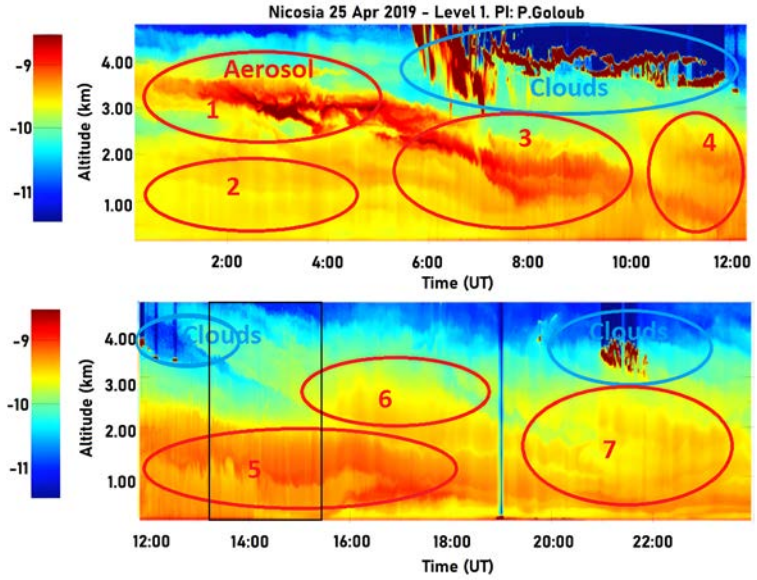

Figure 8. Lidar time series of corrected attenuated atmospheric backscatter (in arbitrary unit) for Nicosia, Cyprus, April 25, 2019. Blue circles indicate the clouds, red circles and numbers (1–7) are marking the aerosol layers.

This information is important for studying aerosol dynamics over some territories, aerosol properties, and sources of aerosol particles. The main part of aerosol pollution is concentrated at planetary boundary level, usually at the altitudes below 1000–2000 m, depending on the topography [39, 40]. The smoke and biomass burning aerosol from powerful wildfires can rise to higher altitudes, as 4–5 km, and ash from volcano eruptions could be able to reach the stratosphere [41,42].

In case of Nicosia, lidar observations cover the entire 2019 year and the event of April 23–25, 2019. Based on these measurements and AERONET sun-photometer data, we provided analysis of the aerosol dust contamination over Nicosia on April 25, 2019. Figure 8 presents the lidar time series of range corrected backscatter signal for Nicosia on April 25, 2019. On April 23, the lidar observations showed a low concentration of aerosol particles in the atmosphere, and on the next day, the backscatter signal increased. Maximum of the backscattering was detected on April 25.

We considered the lidar observations on April 25 in detail, because it was the most polluted day in the April 23–25, 2019 period. Backscatter signal according to lidar observations started to grow up on April 24. When a new aerosol plume arrived at high altitudes (3.5 km, the layer 1 at 01h00m on 25 April, Figure 8), there was already the aerosol pollution below 2 km (Figure 8, the layer 2). The upcoming aerosol layer 1 was located at the altitudes between 3 and 4 km, which are typical for altocumulus clouds. However, clouds were observed after 6h (Figure 8, clouds are marked). At this time aerosol layer 1 went down and mixed with layer 2 and formed layer 3 (Figure 8, the layer 3). Above this layer, the high opacity layer (clouds) was detected at the altitude of 4 km at the 06h–12h period. The changes in aerosol layer 4 (Figure 8, the layer 4) can be explained by wind direction changes at 11h00m. The layer 5 (former layer 4) was dominated until 16h. Then it was separated into layers 6 and 7, which were less saturated than the layer 5 (Figure 8, the layer 5). In addition, in Figure 8 the black rectangle approximately

Preprints (www.preprints.org) | NOT PEER-REVIEWED | Posted: 12 October 2022 doi:10.20944/preprints202210.0176.v1

corresponds to time from 13h15m to 15h20m. The vertical blue line occurred as a consequence of unavailable correct measurements at that time.

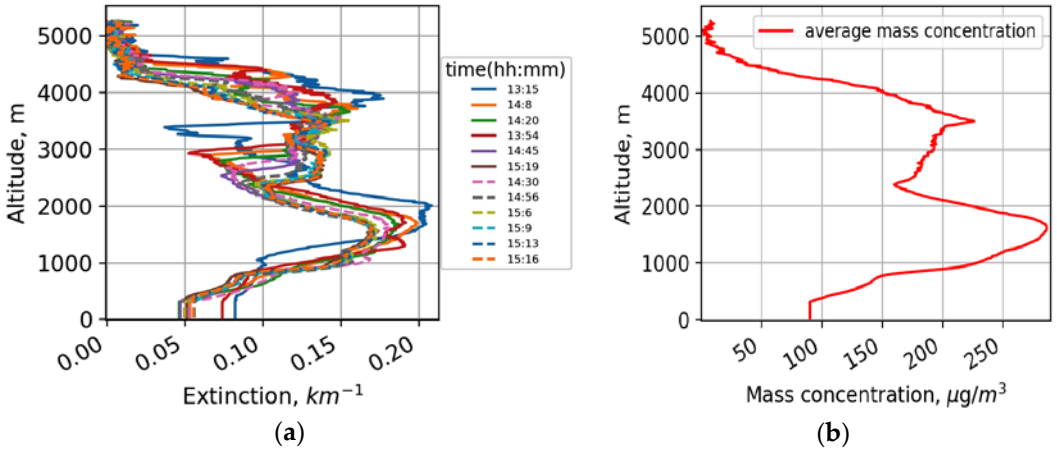

Figure 9. (**a**) Extinction altitude profiles on 25 April from 13h15m to 15h20m and (**b**) average mass concentration altitude profiles on 25 April from 13h15m to 15h20m at Nicosia. Profile time correspond to time that is marked by black square on Figure 8.

In order to determine the aerosol vertical profile of extinction coefficient and mass concentration using lidar data different models of aerosol types and their size distribution should be used. In the AERONET retrieval algorithm, aerosols types are modeled by several modes with a certain aerosol particle size distribution, where each mode is a mixture of homogeneous spherical particles and randomly oriented spheroids [20,22].

Retrieval of extinction profile and effective lidar ratio (the extinction to backscattering ratio) are performed during daytime using methodology [43] that is based on the Klett and Fernald solution [44,45] using BASIC algorithm [46,47] and includes the use of the accurate AOD measurements, such as AERONET. The other AERONET observed aerosol characteristics are the particle diameter (for two modes), the proportion of fine and coarse mode, particle density, and real and imaginary parts of refractive index, which, in synergy with the extinction profile could be used for the calculation of aerosol mass concentration [46]. Lidar retrieval algorithm allows choosing the aerosol type model based on mentioned above aerosol properties: biomass burning, ash, urban-industrial, dust, sea salt, or manually defining.

The extinction profiles in 25 April 2019 are presented in Figure 9a. From 13h15m to 15h20m this day the corrected attenuated atmospheric backscatter (Figure 8, black square) and extinction profiles (Figure 9a) are affected by aerosol plum in the atmosphere without clouds impact. During this time extinction coefficient varies from 0.1 to 0.2. However, the highest detected values were higher than 0.6 on this day. Furthermore, for mass concentration calculations, the following assumptions and observations were used: (1) AERONET observations for refractive index (subsection 3.1, Figure 6.), according to this (2) an assumption that the mineral dust density is approximately 2.6 g m^{-3} [48, 49], (3) dust model for aerosol particles distribution (according to AERONET observations of aerosol size distribution in Figure 5. in subsection 3.1, the dust model is the best for this case), and (4) lidar extinction measurements. The result of the aerosol mass concentration that corresponds to extinction 0.6 is more than 1000 μg m^{-3}. With assumptions that the average particles radius is 1.3 μm (Figure 5.), the calculated average mass concentration from 13h15m to 15h20m is in range 100–300 μg m^{-3} (Figure 9b), which is in few times over that is recommended by Word Health Organization, and higher in comparison to normal conditions for this region. Also, concertation of particles is huge until 5 km, not only at ground level. Two peaks of it at around 1.5 and 3.5 km (Figure 9b) corresponds to marked aerosol plumes as layers 5 and 6 in Figure 8.

3.3. HYSPLIT Calculation of Air Mass Transport and MODIS Observations

Preprints (www.preprints.org) | NOT PEER-REVIEWED | Posted: 12 October 2022 doi:10.20944/preprints202210.0176.v1

For air mass movement calculation, the HYSPLIT model uses meteorological data files from the Global Data Assimilation System (GDAS), which includes a variety of data from different instruments and sources of data: satellites, ground based and aircraft measurements [50]. To study the impact of air mass transport from different regions to Nicosia, the calculations of backward trajectories for different periods and trajectory frequency have been provided. The 6-days backward trajectories are presented in Figure 10a. The trajectory starts every 12 hours and runs 72 hours. That means the latest curve (red) starts at the same time when the earliest (yellow) ends. The altitude for calculation is 500 m above ground level (AGL). The results show the changes of the air mass transport direction from East Europe on 21–24 April to North Africa on 24–25 April. The frequency calculation provides specific information about dominant wind directions and air mass movements over Nicosia. The trajectory frequency option starts a trajectory from a single location (Nicosia) at the height of 500 m AGL every 3 hours. The duration of 72 hours in 3 days for every trajectory is the same that in the previous backward trajectory calculation (Figure 10b).

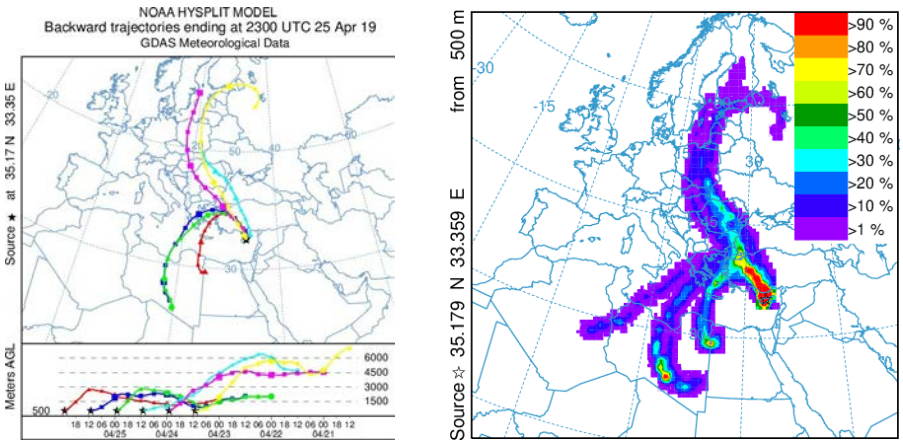

(**a**) (**b**)

Figure 10. (**a**) Backward trajectory of the air mass at 23 UTC and (**b**) trajectory frequency (b) on 25 April 2019, Nicosia, Cyprus. HYSPLIT calculation.

The main part of the upcoming aerosol particles was located at the altitude less than 4 km. The Figure 11a presents the backward trajectories for three different altitudes: 100, 500, and 1000 m AGL. The red and blue lines correspond to 100 and 500 m accordingly, almost matched results in Figure 10a. For higher altitudes (1000 m, green line, Figure 10a) the trajectory is located at western part in comparison with 100 and 500 m trajectories. Trajectories for the 3 previous days before 25 April start over Libya and Egypt that includes the territory of the Sahara Desert (Figure 10, Figure 11a).

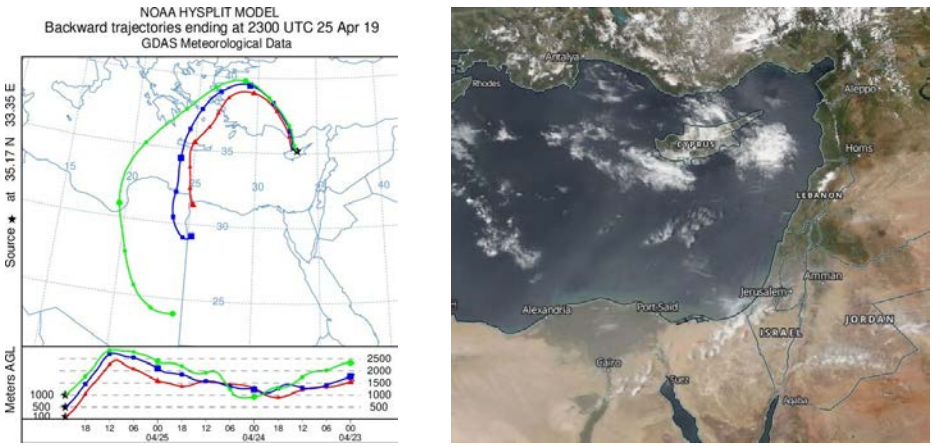

 doi:10.20944/preprints202210.0176.v1

(**a**) (**b**)

Figure 11. (**a**) Backward trajectory of the air mass movement at 23 UTC, and (**b**) MODIS image on 25 July 2019, Nicosia, Cyprus.

In the MODIS satellite image (Figure 11b) the haze of dust is visible over the territory of Egypt and the Mediterranean Sea. This haze corresponds to mineral dust particles transported from Sahara Desert. Comparison with the results of the HYSPLIT calculation confirmed that mineral dust came to Nicosia with air masses transported from the Saharan Desert region.

4. Conclusions

We studied an intense aerosol plume event over Nicosia, Cyprus in the Mediterranean, which is a region where the climate change impact is especially strong. The characteristics of aerosol particles during the high atmospheric aerosol contamination event over Nicosia in April 2019 are considered. The data from the sun-photometer Nicosia AERONET station, the ground-based automatic micro-lidar, the satellite products from the MODIS, and the HYSPLIT back trajectories were used for study. Applying these methods, the aerosol properties, type and possible origin were determined for the April 2019 event.

The AOT, Ångström Exponent, single scattering albedo, refractive index, and size distribution indicate the arrival in the atmosphere over Nicosia in April 2019 of mineral dust particles with AOT at least five times larger (~1.0 at 440 nm, see Figure 3) than background values (~0.2). The backward trajectory analysis clearly shows that the mineral dust arrived from Sahara Desert region and Egypt. The mineral dust aerosol properties in the extreme event of April 25, 2019 were confirmed by lidar measurements and retrievals, by cluster analysis and size distribution (Figures 5, 7 and 9).

Combining automatic photometer and lidar data is the significant approach that allows retrieving extinction, lidar ratio and mass concentration. In addition, the near-real-time (NRT) processing chain combining photometer (day and night) and lidar data for retrieval just mention parameters is being implemented in ACTRIS-France data center. In this work, we use data of CE370 lidar, which are available for 2018-2020. Since 2021, a new automatic, bi-wavelength and depolarized lidar CE376 is in operation at CAO. The device operates in the visible (532 nm, green mode) and/or in the near-infrared (~850 nm, NIR mode) wavelengths with depolarization options. The observations of lidar CE376 provide information about the presence of aspherical particles, such as particles of ashes, sand, cirrus and allow identifying particle sizes [17].

The aerosol conditions in the region around Cyprus were studied in previous works [6,51–53]. These studies show that the mineral dust of Saharan desert from southwest and of the Arabian Peninsula desert from southeast was often transported to atmosphere over Cyprus in several events since 2015. The event of April 25, 2019 was one of the extreme aerosol pollution outbreaks by mineral dust from the Saharan Desert in the atmosphere over Cyprus.

Author Contributions: Conceptualization, Y.Y. and P.G.; methodology, Y.Y., P.G. and G.M.; software, Y.Y.; validation, Y.Y., P.G., I.P. and G.M.; investigation, Y.Y., P.G., I.S., I.P., J.S., M.P., F.M., F.U. and G.M.; writing—original draft preparation, G.M., M.P., P.G. and Y.Y.; writing—review and editing, G.M., I.S., P.G., I.P., J.S., M.P., F.U. and Y.Y.; visualization, Y.Y.; supervision, J.S., G.M. and P.G.; project administration, G.M., I.P. and P.G. Each author contributed to the interpretation and discussion of the results and edited the manuscript. All authors have read and agreed to the published version of the manuscript.

Funding: This research received no external funding.

Institutional Review Board Statement: Not applicable

Informed Consent Statement: Not applicable

Data Availability Statement: Not applicable

Acknowledgments: This work was partly supported by Space Program for 2018-2022 of the National Academy of Sciences of Ukraine through the project 03/22, Ukraine; by Ministry of Education and Science of Ukraine, Kyiv, through the projects 20BF051-02 and BF30-2021; by College of Physics International Center of Future Science, Jilin University, China. The work was partly supported from the European Union's Horizon 2020 research and innovation program under the Marie Skłodowska-Curie grant agreement No 778349 GRASP-ACE and research and innovation program under ACTRIS-2 grant agreement No 654109. We thank Brent Holben (NASA/GSFC) for managing the AERONET program and its sites. Authors also are acknowledged for Climate and Atmosphere Research Centre (CARE-C), Cyprus station, Nicosia, Cyprus. The high quality of AERONET/PHOTONS data were provided by CIMEL sun-photometer calibration performed at the AERONET-EUROPE calibration center. The authors would like also to acknowledge the European Commission Horizon 2020 Program that funded the ERA-PLANET/SMURBS project.

Conflicts of Interest: The authors declare no conflict of interest.

References

1. IPCC, 2022: Climate Change 2022: Impacts, Adaptation, and Vulnerability. Contribution of Working Group II to the Sixth Assessment Report of the Intergovernmental Panel on Climate Change. Pörtner, H.-O.; Roberts, D.C.; Tignor, M.; Poloczanska, E.S.; Mintenbeck, K.; Alegría, A.; Craig, M.; Langsdorf, S.; Löschke, S.; Möller, V.; Okem, A.; Rama B. (eds.). Cambridge University Press. Available online: https://www.ipcc.ch/report/ar6/wg2/ (accessed on 20 March 2022).
2. Chung, C.E.; Chu, J.-E.; Lee, Y.; van Noije, T.; Jeoung, H.; Ha, K.-J.; Marks, M. Global fine-mode aerosol radiative effect, as constrained by comprehensive observations. *Atmos. Chem. Phys*. **2016**, *16*, 8071–8080. https://doi.org/10.5194/acp-16-8071-2016.
3. Lohmann, U.; Feichter, J. Global indirect aerosol effects: a review. *Atmos. Chem. Phys*. **2005**, *5*, 715–737. https://doi.org/10.5194/acp-5-715-2005.
4. Fan, X.; Miao, C.; Duan, Q.; Shen, C.; Wu, Y. Future climate change hotspots under different 21st century warming scenarios. *Earth's Future* **2021**, *9*, e2021EF002027. https://doi.org/10.1029/2021EF002027.
5. Zachariadis, T. Climate Change in Cyprus: Impacts and Adaptation Policies. *Cyprus Economic Policy Review* **2012**, *6*, 21-37.
6. Kaduk, C. Characterization of the optical properties of complex aerosol mixtures observed with a multiwavelength-Raman-polarization lidar during the 6-weeks BACCHUS campaign in Cyprus in spring 2015. Fakultät für Physik und Geowissenschaften der Universität Leipzig Studiengang Meteorologie, Masterarbeit **2017**. Available online: https://www.tropos.de/fileadmin/user_upload/Institut/Abteilungen/Fernerkundung/Daten_PDF/MA_Clara_Kaduk.pdf (accessed on 22 April 2022).
7. Climate data for cities worldwide. Available online: https://en.climate-data.org/ (accessed on 18 March 2022).
8. Prospero, J.M. Long-term measurements of the transport of African mineral dust to the southeastern United States: implications for regional air quality. *J. Geophys. Res*. **1999**, *104*, 15 917–15 927. https://doi.org/10.1029/1999JD900072.
9. Ansmann, A.; Bösenberg, J.; Chaikovsky, A.; Comerón, A.; Eckhardt, S.; Eixmann, R.; Freudenthaler, V.; Ginoux, P.; Komguem, L.; Linne, H.; et al. Long-range transport of Saharan dust to northern Europe: The 11–16 October 2001 outbreak observed with EARLINET. *J. Geophys. Res.-Atmos*. **2003**, *108*, 4783. https://doi.org/10.1029/2003JD003757.
10. Wagner, F.; Bortoli, D.; Pereira, S.; Costa, M.J.; Silva, A.M.; Weinzierl, B.; Esselborn, M.; Petzold, A.; Rasp, K.; Heinold, B.; Tegen, I. Properties of dust aerosol particles transported to Portugal from the Sahara Desert. *Tellus B: Chem. Phys. Meteorol*. **2009**, *61*, 297–306. https://doi.org/10.1111/j.1600-0889.2008.00393.x.
11. Danylevsky, V.; Ivchenko, V.; Milinevsky, G.; Grytsai, A.; Sosonkin, M.; Goloub, Ph.; Li, Z.; Dubovik, O. Aerosol layer properties over Kyiv from AERONET/PHOTONS sunphotometer measurements during 2008–2009. *Int. J. Remote Sens*. **2011**, *32*, 657–669. https://doi.org/10.1080/01431161.2010.517798.
12. Milinevsky, G.; Danylevsky, V. Atmospheric Aerosol Over Ukraine Region: Current Status of Knowledge and Research Efforts. *Front. Environ. Sci*. **2018**, *6*(59), 1–21. https://doi.org/10.3389/fenvs.2018.00059.

13. Amiridis, V.; Balis, D.; Kazadzis, S.; Giannakaki, E.; Papayannis, A.; Zerefos, C. Four years aerosol observations with a Raman lidar at Thessaloniki, Greece, in the framework of European Aerosol Research Lidar Network (EARLINET). *J. Geophys. Res*. **2005**, *110*, D21203. https://doi.org/10.1029/2005JD006190.
14. Papayannis, A.; Mamouri, R.E.; Amiridis, V.; Kazadzis, S.; Perez, C.; Tsaknakis, G.; Kokkalis, P.; Baldasano, J.M. Systematic lidar observations of Saharan dust layers over Athens, Greece in the frame of EARLINET project (2004-2006). *Ann. Geophys*. **2009**, *27*, 3611–3620. https://doi.org/10.5194/angeo-27-3611-2009.
15. Nisantzi, A.; Mamouri, R.E.; Ansmann, A.; Schuster, G.L.; Hadjimitsis, D.G. Middle East versus Saharan dust extinction-to-backscatter ratios. *Atmos. Chem. Phys*. **2015**, *15*, 7071–7084. https://doi.org/10.5194/acp-15-7071-2015.
16. Mamali, D.; Marinou, E.; Sciare, J.; Pikridas, M.; Kokkalis, P.; Kottas, M.; Binietoglou, I.; Tsekeri, A.; Keleshis, C.; Engelmann, R.; et al. Vertical profiles of aerosol mass concentration derived by unmanned airborne in situ and remote sensing instruments during dust events. *Atmos. Meas. Tech*. **2018**, *11*, 2897–2910. https://doi.org/10.5194/amt-11-2897-2018.
17. CIMEL. Available online: www.cimel.fr (accessed on 23 September 2022).
18. Holben, B.N.; Eck, T.F.; Slutsker, I.; Tanré, D.; Buis, J.P.; Setzer, A.; Vermote, E.; Reagan, J.A.; Kaufman, Y.J.; Nakajima, T.; et al. AERONET-A Federated Instrument Network and Data Archive for Aerosol Characterization. *Remote Sens. Environ*. **1998**, *66*, 1–16. https://doi.org/10.1016/S0034-4257(98)00031-5.
19. Holben, B.N.; Kim, J.; Sano, I.; Mukai, S.; Eck, T.F.; Giles, D.M.; Schafer, J.S.; Sinyuk, A.; Slutsker, I.; Smirnov, A. et al. An overview of mesoscale aerosol processes, comparisons, and validation studies from DRAGON networks. *Atmos. Chem. Phys*. **2018**, *18*, 655–671. https://doi.org/10.5194/acp-18-655-2018.
20. AERONET (AErosol RObotic NETwork). Available online: http://aeronet.gsfc.nasa.gov/ (accessed on 28 April 2022).
21. Dubovik, O.; King, M.D. A flexible inversion algorithm for retrieval of aerosol optical properties from Sun and sky radiance measurements. *J. Geophys. Res*. **2000**, *105*, 20673–20696. https://doi.org/10.1029/2000JD900282.
22. Dubovik, O.; Holben, B.; Eck, T.F.; Smirnov, A.; Kaufman, Y.J.; King, M.D.; Tanré, D.; Slutsker, I. Variability of absorption and optical properties of key aerosol types observed in worldwide locations. *J. Atmos. Sci*. **2002**, *59*, 590–608. https://doi.org/10.1175/1520-0469(2002)059<0590:VOAAOP>2.0.CO;2.
23. Dubovik, O.; Sinyuk, A.; Lapyonok, T.; Holben, B.N.; Mishchenko, M.; Yang, P.; Eck, T.F.; Volten, H.; Munoz, O.; Veihelmann, B.; et al. Application of spheroid models to account for aerosol particle nonsphericity in remote sensing of desert dust. *J. Geophys. Res.* **2006**, *111*, D11208. https://doi.org/10.1029/2005JD006619.
24. Giles, D.M.; Sinyuk, A.; Sorokin, M.G.; Schafer, J.S.; Smirnov, A.; Slutsker, I.; Eck, T.F.; Holben, B.N.; Lewis, J.R.; Campbell, J.R.; et al. Advancements in the Aerosol Robotic Network (AERONET) Version 3 database-automated near-real-time quality control algorithm with improved cloud screening for Sun photometer aerosol optical depth (AOD) measurements. *Atmos. Meas. Tech*. **2019**, *12*, 169–209. https://doi.org/10.5194/amt-12-169-2019.
25. Sinyuk, A.; Holben, B.N.; Eck, T.F.; Giles, D.M.; Slutsker, I.; Korkin, S.; Schafer, J.S.; Smirnov, A.; Sorokin, M.; Lyapustin. A. The AERONET Version 3 aerosol retrieval algorithm, associated uncertainties and comparisons to Version 2. *Atmos. Meas. Tech.* **2020**, *13*, 3375–3411. https://doi.org/10.5194/amt-13-3375-2020.
26. Cyprus Atmospheric Observatory. Available online: https://cao.cyi.ac.cy/nicosia/ (accessed on 19 July 2022).
27. The National Ocean Service. Available online: https://oceanservice.noaa.gov/facts/lidar.htm (accessed on 22 April 2022).
28. Popovici, I. E., Goloub, P., Podvin, T., Blarel, L., Loisil, R., Unga, F., Mortier, A., Deroo, C., Victori, S., Ducos, F., Torres, B., Delegove, C., Choël, M., Pujol-Söhne, N., and Pietras, C.: Description and applications of a mobile system performing on-road aerosol remote sensing and in situ measurements, *Atmos. Meas. Tech.* ***2018***, 11, 4671–4691, https://doi.org/10.5194/amt-11-4671-2018.
29. Terra, the EOS Flagship. Available online: http://terra.nasa.gov/about (accessed on 20 March 2022).
30. MODIS (Moderate Resolution Imaging Spectroradiometer). Available online: https://modis.gsfc.nasa.gov/about/index.php (accessed on 20 March 2022).
31. Witte, J.C.; Douglass, A.R.; da Silva, A.; Torres, O.; Levy, R.; Duncan, B.N. NASA A-Train and Terra observations of the 2010 Russian wildfires. *Atmos. Chem. Phys*. **2011**, *11*, 9287–9301. https://doi.org/10.5194/acp-11-9287-2011.
32. Draxler, R.R.; Hess, G.D. An overview of the HYSPLIT 4 modeling system for trajectories, dispersion, and deposition. *Aust. Meteor. Mag*. **1997**, *47*, 295–308.
33. Stein, A.F.; Draxler, R.R.; Rolph, G.D.; Stunder, B.J.B.; Cohen, M.D.; Ngan, F. NOAA's HYSPLIT atmospheric transport and dispersion modeling system. *Bull. Amer. Meteor. Soc*. **2015**, *96*, 2059–2077. https://doi.org/10.1175/BAMS-D-14-00110.1.
34. Global Data Assimilation System (GDAS). National Oceanic and Atmospheric Administration. Available online: https://data.noaa.gov/dataset/dataset/global-data-assimilation-system-gdas (accessed on 13 February 2022).

35. Maring, H.; Savoie, D.L.; Izaguirre, M.A.; Custals, L.; Reid, J.S. Mineral dust aerosol size distribution change during atmospheric transport. *J. Geophys. Res.-Atmos*. **2003**, *108*, 8592. https://doi.org/10.1029/2002JD002536.
36. Zhang, Y.; Li, Z.; Zhang, Y.; Li, D.; Qie, L.; Che, H.; Xu, H. Estimation of aerosol complex refractive indices for both fine and coarse modes simultaneously based on AERONET remote sensing products. Atmos. Meas. Tech. **2017**, *10*, 3203–3213. https://doi.org/10.5194/amt-10-3203-2017.
37. Omar, A.H.; Won, J.-G.; Winker, D.M.; Yoon, S.-C.; Dubovik, O.; McCormick, M.P. Development of global aerosol models using cluster analysis of Aerosol Robotic Network (AERONET) measurements. *J. Geophys. Res*. **2005**, *110*, D10S14. https://doi.org/10.1029/2004JD00487.
38. Szkop, A.; Pietruczuk, A.; Posyniak, M. Classification of aerosol over Central Europe by cluster analysis of aerosol columnar optical properties and backward trajectory statistics. *Acta Geophys*. **2016**, *64*, 2650–2676. https://doi.org/10.1515/acgeo-2016-0112.
39. Liu, S.; Liang X.-Z. Observed diurnal cycle climatology of planetary boundary layer height Shuyan. *J. Climate* **2010**, *23*(21), 5790–5809. https://doi.org/10.1175/2010JCLI3552.1.
40. Palm, S.P.; Selmer, P.; Yorks, J.; Nicholls, S.; Nowottnick, E. Planetary Boundary Layer Height Estimates From ICESat-2 and CATS Backscatter Measurements. *Front. Remote Sens*. **2021**, *2*, 716951. https://doi.org/10.3389/frsen.2021.716951.
41. Papanikolaou, C.-A.; Papayannis, A.; Mylonaki, M.; Foskinis, R.; Kokkalis, P.; Liakakou, E.; Stavroulas, I.; Soupiona, O.; Hatzianastassiou, N.; Gavrouzou, M.; Kralli, E.; Anagnou, D. Vertical Profiling of Fresh Biomass Burning Aerosol Optical Properties over the Greek Urban City of Ioannina, during the PANACEA Winter Campaign. *Atmosphere* **2022**, *13*, 94. https://doi.org/10.3390/atmos13010094.
42. Mona, L.; Amodeo, A.; D'Amico, G.; Giunta, A.; Madonna, F.; Pappalardo, G. Multi-wavelength Raman lidar observations of the Eyjafjallajökull volcanic cloud over Potenza, southern Italy. *Atmos. Chem. Phys*. **2012**, *12*, 2229–2244. https://doi.org/10.5194/acp-12-2229-2012.
43. Leon, J.-F.; Derimian, Y.; Chiapello, I.; Tanre, D.; Podvin, T.; Chatenet, B.; Diallo, A.; Deroo, C. Aerosol vertical distribution and optical properties over M'Bour (16.96°W; 14.39°N), Senegal from 2006 to 2008. *Atmos. Chem. Phys*. **2009**, *9*, 9249–9261. https://doi.org/10.5194/acp-9-9249-2009.
44. Klett, J.D. Stable analytical inversion solution for processing lidar returns. *Appl. Opt*. **1981**, *20*, 211-220. https://doi.org/10.1364/AO.20.000211.
45. Fernald, F.G. Analysis of atmospheric LIDAR observations: some comments. *Appl. Opt*. **1984**, *23*, 652–653. https://doi.org/10.1364/ao.23.000652
46. Mortier, A.; Goloub, P.; Podvin, T.; Deroo, C.; Chaikovsky, A.; Ajtai, N.; Blarel, L.; Tanre, D.; Derimian, Y. Detection and characterization of volcanic ash plumes over Lille during the Eyjafjallajökull éruption. *Atmos. Chem. Phys*. **2013**, *13*, 3705-3720. https://doi.org/10.5194/acp-13-3705-2013.
47. Mortier, A.: Tendances et variabilites de l'aerosol atmospherique a l'aide du couplage Lidar/Photometre sur les sites de Lille et Dakar, University of Lille, ***2013***.
48. Linke, C., Möhler, O., Veres, A., Mohácsi, Á., Bozóki, Z., Szabó, G. and Schnaiter, M.: Optical properties and mineralogical composition of different Saharan mineral dust samples: A laboratory study. *Atmos. Chem. Phys.*, ***2006***, 6(11), 3315–3323. https://doi.org/10.5194/acp-6-3315-2006.
49. Kandler, K., Lieke, K., Benker, N., Emmel, C., Küpper, M., Müller-Ebert, D., Ebert, M., Scheuvens, D., Schladitz, A., Schütz, L. and Weinbruch, S.: Electron microscopy of particles collected at Praia, Cape Verde, during the Saharan Mineral Dust Experiment: Particle chemistry, shape, mixing state and complex refractive index. *Tellus, Ser. B Chem. Phys. Meteorol.*, ***2011***, 63(4), 475–496. https://doi.org/10.5194/acp-6-3315-2006.
50. Draxler, R.R.; Hess, G.D. An overview of the HYSPLIT 4 modeling system for trajectories, dispersion, and deposition. *Aust. Meteor. Mag*. **1997**, *47*, 295–308.
51. Gong, X.; Wex, H.; Müller, T.; Wiedensohler, A.; Höhler, K.; Kandler, K.; Ma, N.; Dietel, B.; Schiebel, T.; Möhler, O.; Stratmann, F. Characterization of aerosol properties at Cyprus, focusing on cloud condensation nuclei and ice-nucleating particles. *Atmos. Chem. Phys*. **2019**, *19*, 10883–10900. https://doi.org/10.5194/acp-19-10883-2019.
52. Calmer, R.; Roberts, G.C.; Sanchez, K.J.; Sciare, J.; Sellegri, K.; Picard, D.; Vrekoussis, M.; Pikridas, M. Aerosol–cloud closure study on cloud optical properties using remotely piloted aircraft measurements during a BACCHUS field campaign in Cyprus. *Atmos. Chem. Phys*. **2019**, *19*, 13989–14007. https://doi.org/10.5194/acp-19-13989-2019.
53. Retalis, A.; Hadjimitsis, D.G.; Michaelides, S.; Tymvios, F.; Chrysoulakis, N.; Clayton, C.R.I.; Themistocleous, K. Comparison of aerosol optical thickness with in situ visibility data over Cyprus. *Nat. Hazards Earth Syst. Sci*. **2010**, *10*, 421–428. https://doi.org/10.5194/nhess-10-421-2010.